ORIGINAL ARTICLE

A Wirelessly Rechargeable Integrated System for Automatic Sleep Monitoring in a Smart Oral Appliance

Kun-Ying Yeh[1], Kuan Tang[1], Chun-Chang Wu[1], Chia-Ming Chang[1], Tao Wang[2], Yunn-Jy Chen[3], Wen-Cheng Kuo[4], Yao-Joe Yang[1], and Shey-Shi Lu[1,*]

[1]*National Taiwan University, Taipei, Taiwan*
[2]*Chang Gung University, Taoyuan, Taiwan*
[3]*National Taiwan University Hospital, Taipei, Taiwan*
[4]*National Kaohsiung First University of Science and Technology, Kaohsiung, Taiwan*
(**Received** 1 December 2016; **Accepted** 12 March 2017; **Published on line** 1 June 2017)
*Corresponding author: sslu@ntu.edu.tw
DOI: 10.5875/ausmt.v7i2.1327

Abstract: A system integrating temperature, pressure and voice sensors is proposed for a smart oral appliance for use in diagnosing and alleviating obstructive sleep apnea (OSA). Using sealed bio-compatible packaging for intraoral use, this system is also capable of wireless charging and data transmission. This proposed design aims to enhance the effectiveness and convenience of OSA treatment.

Keywords: smart oral appliance, sleep monitoring, sleep apnea, wireless charging

Introduction

Sleep apnea is a serious sleep disorder that occurs when a person's breathing is interrupted one or more times during sleep. The most common type of sleep apnea is obstructive sleep apnea (OSA), which occurs when the throat muscles intermittently relax and block the airway [1]. More than 3% of people globally suffer from OSA [2]. Although OSA is not fatal, it can lead to many health problems including high blood pressure, stroke, heart failure, diabetes, and depression [3]. Furthermore, untreated OSA reduces performance in everyday activities and can lead to increased risk of potentially dangerous accidents [4].

Oral appliance therapy is an effective treatment option for snoring and obstructive sleep apnea [5]. It holds the tongue or supports the jaw in a forward position, which tightens the soft tissue and muscles of the upper airway to prevent airway obstruction. This therapy is popular with patients because it is quiet, comfortable, easy to wear, convenient for travel, and easy to care for. However, many slight alterations are required to fit the needs of each patient, thus reducing efficiency. This paper presents an integrated system capable of automatic continuous sleep monitoring in an oral appliance to intelligently collect essential bio-information and improve therapy effectiveness and efficiency.

The following sections introduce the system application scenario and proposed architecture. The sub-block circuit design and simulation results are then addressed, followed by conclusions.

System Architecture

Figure 1 shows the application scenario of the proposed system. The proposed smart oral appliance is worn by the OSA patient each night during sleep, assuming an average of 7-8 hours of sleep each night. During usage, the intraoral device alleviates OSA symptoms and automatically collects physiological data. In the morning, the user cleans the device and replaces it on its charging base where the physiological data is retrieved for transmission to the user's personal computer and cloud storage applications, thus allowing the clinician

to access current intraoral data to inform continuing treatment decisions.

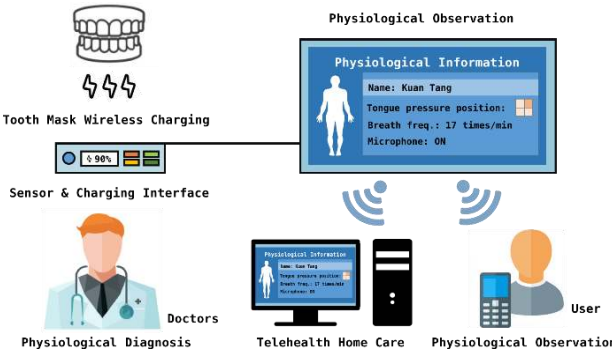

Figure 1. Application scenario of the proposed system.

Figure 2 shows the block diagram of the proposed system, which consists of an analog front-end circuit (AFE), a 10-bit analog-to-digital converter (ADC), a power management circuit, a low-power medical implant communication service (MICS) band transmitter, and a digital micro-controller unit (MCU). The analog front-end circuit operates in either temperature or pressure detection mode to process corresponding signals from the temperature or pressure sensors. Temperature sensing sift out invalid data, while pressure sensing determines tongue positioning, which is significant for OSA diagnosis. Successive-approximation-register (SAR) topology is selected to achieve ultra-low power consumption with a decent effective number of bits (ENOB). On-off-keying (OOK) modulation is chosen for the device's wireless transmitter for its simplicity and low power consumption.

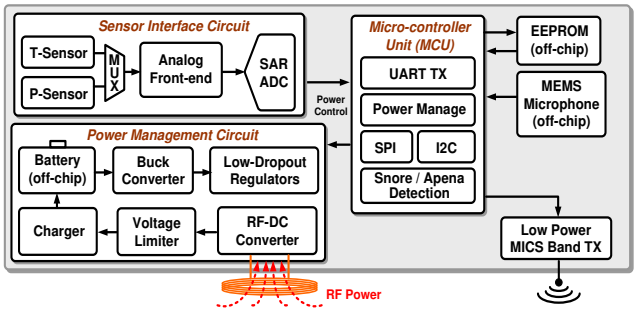

Figure 2. Block diagram of the proposed system.

The power management circuit includes an RF-DC converter, a voltage limiter, a bandgap reference, and several low-dropout regulators (LDOs). The rechargeable Li-ion battery should provide continuous 8 hours of operation. The device is sealed in bio-compatible packaging for intraoral use, and thus is designed to harvest power wirelessly from the RF-DC converter, charging the battery through the on-chip charger. A buck converter is also integrated to increase power transition efficiency. Each of the power domains in this system is allocated an LDO to ensure superior power supply. The digital MCU handles all the signals, and temporarily saves the data in the EEPROM before sending it to the transmitter for wireless transmission. An MEMS microphone is also integrated for snore audio recording and feature extraction. High volume snoring and incidents of sleep apena are recorded with corresponding time stamps for diagnosis reference.

Sub-block Circuit Design

A. Sensor Interface Circuit

The sensor interface circuit [6] consists of an analog front-end circuit and a 10-bit SAR ADC. The analog front-end circuit uses a low power and high gain operational amplifier (OPamp) to form a resistor feedback amplifier, whose loop gain is well defined by the resistor ratio [7-10]. Figue 3 shows the schematic of AFE circuit. Temperature and pressure sensors are integrated in this circuit, and the two detection modes can be toggled through the MUX settings.

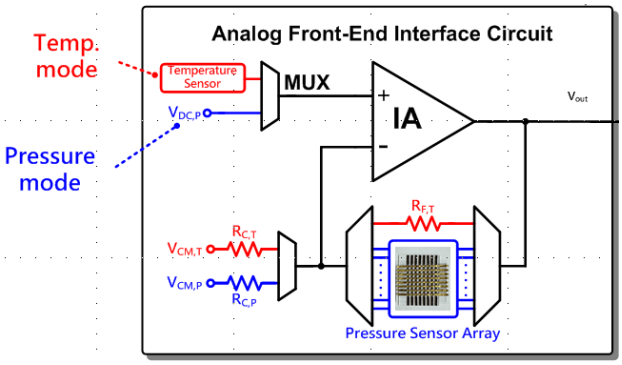

Figure 3. The schematic of analog front-end circuit.

The pressure sensor must be sensitive to 10kPa in order to accurately sense tongue movement. We thus select a tunneling piezoresistive sensor with ultra-high sensitivity of -0.5/kPa [11]. Figure 4 shows the schematic and cross-sectional view of this sensor. When the pressure is applied, the contact area between the two microdome structures made of multi-wall carbon nanotubes and poly-dimethylsiloxane (MWCNT and PDMS) conductive polymer increases significantly, which in turn changes the tunneling resistance. This change of resistance value is multiplied and converted to a voltage signal in the resistor feedback amplifier (AFE). For this application, an 8 x 8 sensor array is designed to determine tongue positioning as accurately as possible.

ADC design requirements prioritizes robustness and low power consumption. The ADC processes bio-signals from changes of intraoral temperature and tongue position, which are in the low-frequency band, and thus does not prioritize speed or resolution. According to these considerations, a conventional SAR ADC is an appropriate choice [12-14].

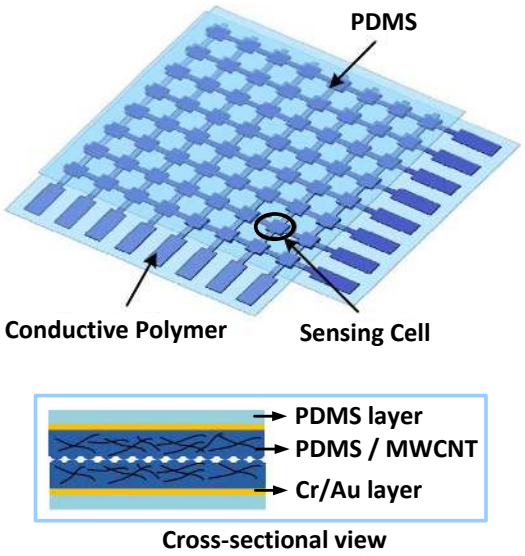

Figure 4. The schematic and cross-sectional view of tunneling piezoresistive pressure sensor.

B. *Micro-controller Unit (MCU)*

The MCU in this system is responsible for the following tasks: (1) arranging digitized signals from the sensors in RS232 format and sending them to the wireless transmitter; (2) controlling all on-chip switches to complete specific operations on demand, including the management of LDOs for different circuit blocks and the scanning of pressure sensor array; (3) performing I2C conversion to communicate with the off-chip EEPROM for data storage; (4) detecting snoring and sleep apnea from acoustic signals from the MEMS microphone [15-17].

C. *Power Management Circuit*

The power management circuit comprises a RF-DC converter, a voltage limiter, a bandgap reference, and several low-dropout regulators (LDOs). Figure 5 shows the block diagram and operation illustration of the power management circuit. This circuit performs two functions: (1) wireless power harvesting and battery charging and (2) voltage level step-down and regulation.

Figure 5(a) presents the block diagram and operation for the first part of this circuit. The RF-DC converter harvests the external wireless power, and its output is limited to an appropriate voltage level by the voltage limiter. After regulation, the charger charges the Li-ion battery with the harvested energy.

A smooth control circuit is integrated in the charger to simultaneously achieve fast charging and prevent battery damage from undercharging or overcharging [19]. The battery will be charged to about 3V with a constant current (~6.8mA) and then switched to a constant voltage stage to finish at 3.6V.

Figure 5(b) shows the block diagram and circuit operation after the battery. A rechargeable battery is used to guarantee a qualified and sustained power supply. However, most compact commercial batteries have output voltages of approximately 3.6V, while the operating voltage of the standard 0.18um CMOS process is 1.8V. A DC-DC buck converter is used to effectively increase voltage step-down efficiency [20-21]. The regulator consumes a voltage headroom of 0.3V, thus the output voltage of the buck converter is set to 2.1V and supplies several regulators specific to different circuit blocks.

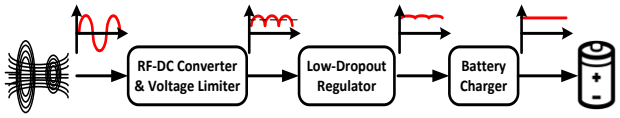

Figure 5. Block diagram and operation of wireless charging circuit.

D. *Low Power MICS band Transmitter*

The MICS band transmitter delivers the sensed bio-information wirelessly to the charging interface and then to the cloud. As shown in Fig. 6, this circuit is composed of a quench generator, a voltage-control oscillator (VCO), and a buffer. When TX in data arrives, the corresponding quench signal is generated to modulate the VCO. The VCO then begins to oscillate when the quench equals 1 and turns off when it equals 0 [18]. The buffer enhances the VCO output signals and ensures sufficient output power to the wireless transmitter.

Figure 6. Block diagram and operation of circuits after the battery.

Simulation Results

The proposed system is designed and implemented in a single chip by using 0.18um standard CMOS process, with several external components such as a pressure sensor array and a MEMS microphone.

Figure 7 shows the simulated open-loop AC response of the OPamp in the AFE circuit. Process variation is also considered, and the simulation results are summarized in Table 1. This OPamp has an 80dB DC gain, 65 degree phase margin, and 4.5 MHz unit-gain bandwidth in the open-loop AC response. The variation in Table 1 at different process corners (typical-typical, fast-fast, slow-slow) is well-controlled, meaning the circuit robustness is ensured.

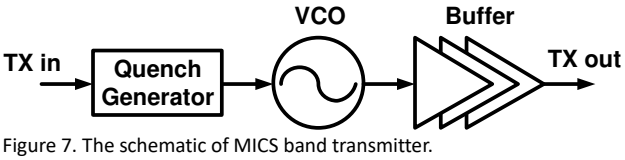

Figure 7. The schematic of MICS band transmitter.

Figure 8 shows the simulated ADC output spectrum at 200KS/s with Nyquist input, and the results at the process corners are summarized in Table 2. In brief, the dynamic behavior of the ADC with Nyquist input is verified by the simulations. The results of signal to noise-and-distortion ration (SNDR) and effective number of bits (ENOB) show decent performance at three different process corners.

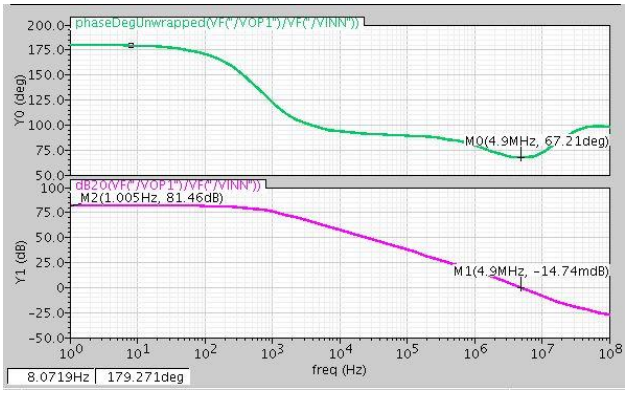

Figure 8. Simulated opened-loop AC response of the OPamp in AFE circuit.

Table 1. Performance summary of the OPamp in AFE.

	Process corner		
	TT	**FF**	**SS**
DC Gain (dB)	81.4	80.5	82.3
Phase margin (deg)	67.2	66.9	68.1
Unit-gain BW (MHz)	4.9	4.9	4.9

Table 2. Performance summary of ADC.

	Process corner		
	TT	**FF**	**SS**
Input freq (Hz)	100k	100k	100k
SNDR (dB)	60.05	59.22	61.18
ENOB (bit)	9.68	9.54	9.87

Figure 9 presents the simulated temperature dependency of the output voltages in the on-chip sensor and AFE circuit. The curves in Fig. 9 are approximately linear from 0 to 100°C and saturate slightly at higher temperatures. However, the detection range of the temperature sensor in this system is about 20 to 50°C, and the curves are quite linear in this range and are thus suitable for system use. When pressure is applied, the equivalent resistance of the pressure sensor may vary from several tens of kilo-ohms to several mega-ohms. Figure 10 shows the simulated feedback resistance dependency of the output voltage in the AFE circuit. In this simulation, the feedback resistance is scanned from 1 kilo-ohm to 10 mega-ohms to replicate the pressure-induced resistance variation, and the signals of output voltage variation appear in the kilo-ohm range, indicating that the induced pressure can be converted to the corresponding output voltage signal of AFE circuit.

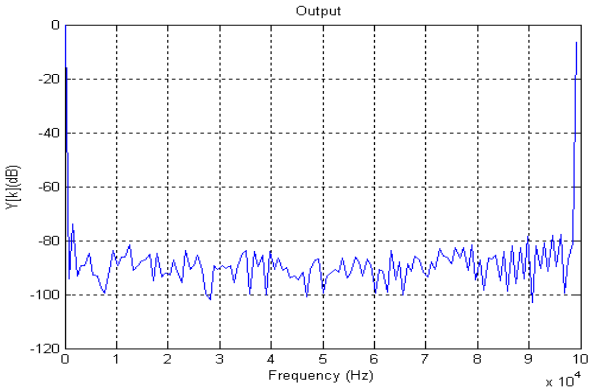

Figure 9. Simulated ADC output spectra at 200KS/s with Nyquist input.

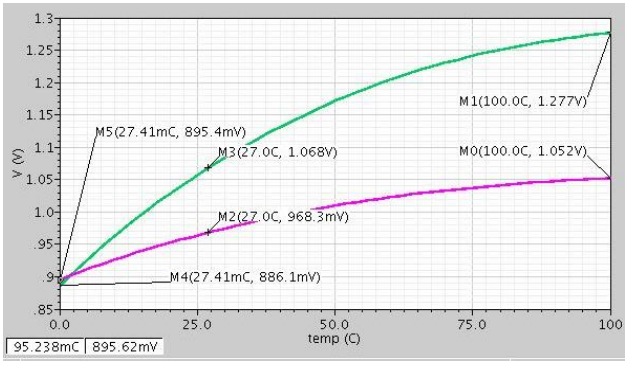

Figure 10. Simulated temperature dependency of the output voltage in the on-chip sensor.

Wireless charging requires the harvesting of external RF power. Figure 11 shows the simulated RF-DC circuit outputs before and after the V-limter. RF power is successfully converted to DC voltage and limited to around 4.2V after the V-limiter. This voltage will support the charger in recharging the Li-ion battery after the regulation. Figure 12 shows the conceptual schematic of the charger. The charger fist operates in contant current mode for rapid charging. It also monitors the output voltage by resistive feedback and will smoothly switch to contant voltage mode when the output voltagle reaches a specific value to prevent damage from overcharging. Figure 13 presents the simulated charging voltage and current in the charger. The output voltage in the charger is gradually recharged to 3.6V and the current stays nearly constant until the output reaches its final value. The DC-DC buck converter design is crucial to achieving the voltage step-down and good power efficiency. Figure 14 presents the simulated output voltage and current of the buck converter. The converter's output voltage starts from zero and smoothly settles to the expected value of 2.1V. In the middle of the simulation, the load current switches from 500uA to 5mA and the output voltage stays nearly contant (~120mV difference), showing good load regulation. When the load current switches to the previous value of 500uA, the output voltage reverts to the

previous level as well, with a transient time of less than 1ms.

Figure 15 shows the simulated output wavefrom of the wireless transmitter in operation. The transmitter exhibits an oscillation of 403 MHz while delivering data 1, and a dc voltage while delivering data 0. Simulation results indicate the proposed integrated system is well designed and implemented in standard 0.18um CMOS process. Figure 16 shows the layout with a total chip area of 3.16 mm x 3.09mm. All results are summarized in Table 3.

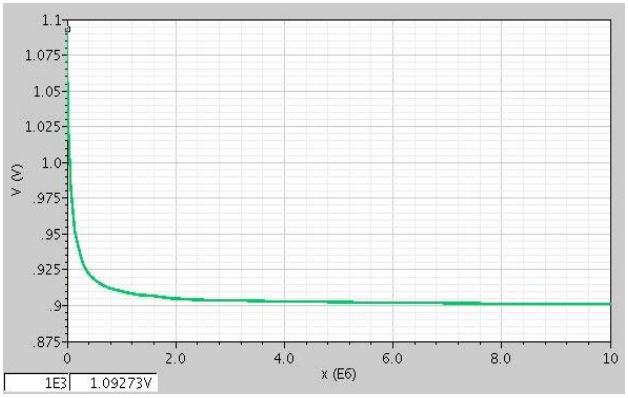

Figure 11. Simulated feedback resistance dependency of the output voltage in the AFE circuit.

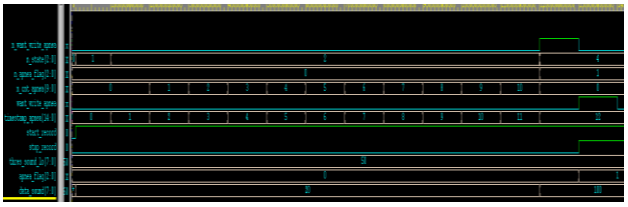

Figure 12. Simulated function test of the overall MCU circuit.

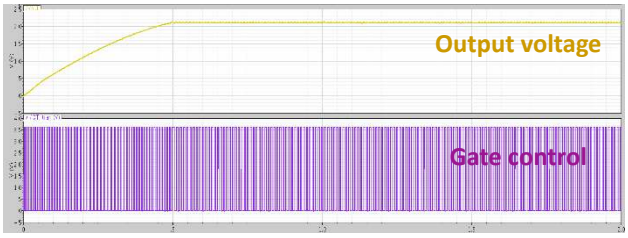

(a)

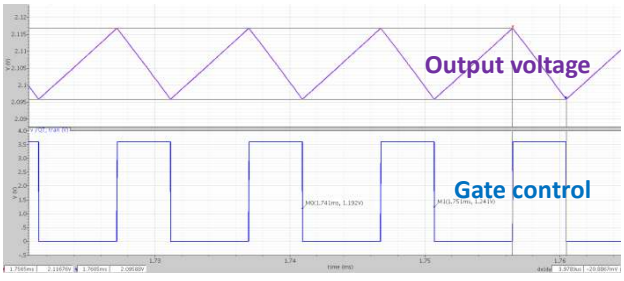

(b)

Figure 13. (a) Simulated start-up transient of buck converter. (b) Simulated steady state of buck converter.

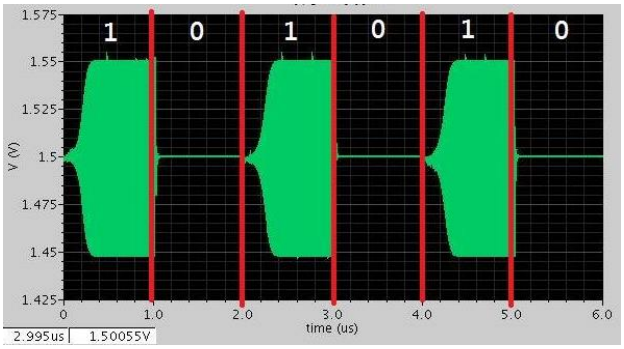

Figure 14. Simulated output waveform of the wireless transmitter.

Figure 15. Layout of the proposed integrated system chip.

Conclusion

Oral appliance therapy is a convenient treatment option for snoring and obstructive sleep apnea. The proposed system automatically monitors user sleep and considerably improves treatment efficiency. Clinicians can access collected bio-information by wireless transmission and cloud-based applications, thus presenting diagnosis and treatment benefits to obstructive sleep apnea sufferers.

Acknowledgment

The authors acknowledge support from the Ministry of Science and Technology (103-2221-E-002-196-MY2) and chip fabrication assistance from the National Chip Implementation Center (CIC).

References

[1] J. Coleman, “Complications of snoring, upper airway resistance syndrome, and obstructive sleep apnea syndrome in adults,” *Otolaryngologic Clinics of*

North America, vol. 32, no. 2, pp. 223-234, 1999. doi: 10.1016/S0030-6665(05)70126-2

[2] T. Young, M. Palta, J. Dempsey, J. Skatrud, S. Weber, and S. Badr, "The occurrence of sleep disordered breathing among middle-aged adults," *New England Journal of Medicine*, vol. 328, no. 17, pp. 1230-1235, 1993. doi: 10.1056/NEJM199304293281704

[3] Standards of Practice Committee of the American Sleep Disorders Association, "Practice parameters for the indications for polysomnography and related procedures," *Sleep*, vol. 20, no. 2, pp.406-422, 1997.

[4] T. Gislason and B. Benediktsdottir, "Snoring, apnea episodes and nocturnal hypoxemia among children 6 months to 6 years old: an epidemiologic study of lower limit of prevalence," *Chest*, vol.107, no. 4, pp.963-966, 1995. doi: 10.1378/chest.107.4.963

[5] A. Pitsis, et al., "Effect of vertical dimension on efficacy of oral appliance therapy in obstructive sleep apnea", *American journal of respiratory and critical care medicine*, vol. 166, no. 6, pp. 860-864, 2002. doi: 10.1164/rccm.200204-342OC

[6] C.-W. Huang, et al., "A fully integrated hepatitis B virus DNA detection SoC based on monolithic polysilicon nanowire CMOS process", in proceeding of *Symposium on VLSI Circuits*, Honolulu, HI, USA, June 13-15, 2012. doi: 10.1109/VLSIC.2012.6243821

[7] R. F Yazicioglu, Kim Sunyoung, T. Torfs, Kim Hyejung, and C. V. Hoof, "A 30 uW Analog Signal Processor ASIC for Portable Biopotential Signal Monitoring," *IEEE Journal of Solid-State Circuits*, vol.46, no.1, pp.209-223, 2011. doi: 10.1109/JSSC.2010.2085930

[8] W.-S. Liew, X.-D. Zou, L.-B. Yao, and Y. Lian, "A 1-V 60-µW 16-channel interface chip for implantable neural recording," in proceeding of *IEEE Custom Integrated Circuits Conference*, Rome, Italy, Sept. 13-16, 2009. doi: 10.1109/CICC.2009.5280795

[9] R. F. Yazicioglu, P. Merken, R. Puers, and C. V. Hoof, "A 60 uW 60 nV/ $\sqrt{}$ Hz Readout Front-End for Portable Biopotential Acquisition Systems," *IEEE Journal of Solid-State Circuits*, vol.42, no.5, pp.1100-1110, 2007. doi: 10.1109/JSSC.2007.894804

[10] R. F. Yazicioglu, P. Merken, R. Puers, and C. V. Hoof, "A 200 uW Eight-Channel EEG Acquisition ASIC for Ambulatory EEG Systems," *IEEE Journal of Solid-State Circuits*, vol.43, no.12, pp.3025-3038, 2008. doi: 10.1109/ISSCC.2008.4523108

[11] C.-W. Ma, C.-M. Chang, T.-H. Lin, and Y.-J. Yang, "Highly Sensitive Tactile Sensing Array Realized Using a Novel Fabrication Process with Membrane Filters," *Journal of Mircoelectromechanical Systems,* vol. 24, no.6, pp. 2062–2070, 2015. doi: 10.1109/JMEMS.2015.2469252

[12] H. Hong and G. Lee, "A 65-fJ/conversion-step 0.9-V 200kS/s rail-to-rail 8-bit successive approximation ADC," *IEEE Journal of Solid-State Circuits*, vol. 42, no. 10, pp. 2161-2168, 2007. doi: 10.1109/JSSC.2007.905237

[13] C.-C. Liu, S.-J. Chang, G.-Y. Huang, and Y.-Z. Lin; "A 10-bit 50-MS/s SAR ADC With a Monotonic Capacitor Switching Procedure," *IEEE Journal of Solid-State Circuits*, vol. 45, no. 4, pp. 731-740, 2010. doi: 10.1109/JSSC.2010.2042254

[14] D. A. Johns and K. Martin, *Analog Integrated Circuit Design*, New York: John Wiley & Sons, 1997.

[15] J.-S. Park, W.-P. Jeong, H. Mahmoodi-Meimand, Y.-T. Wang, H. Choo, and K. Roy, "Computation sharing programmable FIR filter for low-power and high-performance applications," *IEEE Journal of Solid-State Circuits*, vol.39, no.2, pp. 348- 357, 2004. doi: 10.1109/JSSC.2003.821785X

[16] M. Bahoura and H. Ezzaidi, "FPGA-implementation of wavelet-based denoising technique to remove power-line interference from ECG signal," in proceeding of *IEEE International Conference on Information Technology and Applications in Biomedicine*, Corfu, Greece, Nov. 3-5, 2010. doi: 10.1109/ITAB.2010.5687709

[17] X. Liu, Y.-J. Zheng, M.-W. Phyu, B. Zhao, M. Je, and X.-J. Yuan, "Multiple Functional ECG Signal is Processing for Wearable Applications of Long-Term Cardiac Monitoring," *IEEE Transactions on Biomedical Engineering*, vol.58, no.2, pp.380-389, 2011. doi: 10.1109/TBME.2010.2061230

[18] M. K. Raja and Y.-P. Xu, "A 52 pJ/bit OOK transmitter with adaptable data rate," in proceeding of *IEEE Asian Solid-State Circuits Conference,* Fukuoka, Japan, Nov. 3-5, 2008. doi: 10.1109/ASSCC.2008.4708797

[19] C.-H. Lin, et al., "A Li-Ion Battery Charger With Smooth Control Circuit and Built-In Resistance Compensation for Achieving Stable and Fast Charging", *IEEE Transactions on Circuits and Systems*, vol. 57, no. 2, pp.506-517, 2010. doi: 10.1109/TCSI.2009.2023830

[20] G.-H. Zhou and J.-P. Wang, "Constant-Frequency Peak-Ripple-Based Control of Buck Converter in CCM: Review, Unification, and Duality", *IEEE Transactions in Industrial Electronics*, vol.61, no. 3, pp. 1280-1291, 2014.

doi: 10.1109/TIE.2013.2257143

[21] M.-R. Leng and S.-G. Xu, "The Novel Ripple-Based I2 Type Control Technique for Buck Converters with Constant Current Output", in proceeding of *IEEE 8th International Power Electronics and Motion Control Conference*, Hefei, China, May 22-26, 2016.
doi: 10.1109/IPEMC.2016.7512694

[22] M. Kuhl, et al. "A telemetric stress-mapping CMOS chip with 24 FET-based stress sensors for smart orthodontic brackets," in proceeding of *IEEE International Solid-State Circuits Conference*, San Francisco, CA, Feb. 20-24, 2011.
doi: 10.1109/ISSCC.2011.5746240

[23] P. Gieschke, et al. "CMOS integrated stress mapping chips with 32 N-type or P-type piezoresistive field effect transistors." In proceeding of *IEEE 22nd International Conference on Micro Electro Mechanical Systems*, Sorrento, Italy, Jan. 25-29, 2009.
doi: 10.1109/MEMSYS.2009.4805496

[24] M. Suster, et al. "A wireless strain sensing microsystem with external RF power source and two-channel data telemetry capability." In proceeding of *IEEE International Solid-State Circuits Conference. Digest of Technical Papers*, San Francisco, CA, Feb. 11-15, 2007.
doi: 10.1109/ISSCC.2007.373453